PAPER

Check for updates

Advanced mixed-linker UiO-66 MOFs as high-performance functional materials for removing emerging contaminants: DFT-guided design and real wastewater validation

Vu Thi Hoa [ID] *

The persistent contamination of aquatic environments by emerging organic pollutants (EOPs) such as bisphenol A (BPA) and tetracycline (TC) poses significant threats to ecosystems and human health. Herein, we report a computationally guided strategy for designing mixed-linker metal–organic frameworks (ML-MOFs) with enhanced selectivity toward BPA and TC removal. By systematically incorporating amino-functionalized and pyridine-functionalized terephthalic acid linkers alongside conventional BDC linkers into UiO-66 topology, we engineered ML-MOFs with tailored binding sites. Density functional theory (DFT) calculations revealed that amino- and pyridine-functionalized linkers strengthen pollutant binding through $\pi-\pi$ stacking, hydrogen bonding, and electrostatic interactions, with adsorption energies of -89.4 kJ mol^{-1} (BPA) and -102.7 kJ mol^{-1} (TC), significantly exceeding those of parent UiO-66 (-52.3 and -61.8 kJ mol^{-1}, respectively). The optimized ML-MOF (UiO-66-NH$_2$/Py, 1:1:2 BDC:NH$_2$–BDC:Py–BDC ratio) demonstrated exceptional adsorption capacities of 385 mg g^{-1} for BPA and 428 mg g^{-1} for TC, outperforming commercial adsorbents (activated carbon: 156 mg per g BPA and 189 mg per g TC). X-ray photoelectron spectroscopy (XPS) and Fourier-transform infrared spectroscopy (FTIR) analyses validated the computational predictions of specific binding mechanisms. Remarkably, the ML-MOF retained >92% capacity after five regeneration cycles and exhibited minimal capacity loss (≤15%) in industrial wastewater matrices. Competitive adsorption studies and column breakthrough experiments confirmed practical applicability. This synergistic computational–experimental approach provides a robust framework for rational MOF design targeting persistent environmental contaminants.

Sustainability spotlight

Our research on mixed-linker UiO-66 metal–organic frameworks (ML-MOFs) represents a major advancement in sustainable water treatment technologies. By integrating computational design (DFT) with experimental validation, the study presents a high-performance, regenerable adsorbent that efficiently removes persistent pollutants—bisphenol A (BPA) and tetracycline (TC)—from contaminated water. The optimized UiO-66-NH$_2$/Py MOF achieves pollutant removal efficiencies exceeding 90%, even in real industrial wastewater, while retaining an adsorption capacity of over 92% over multiple regeneration cycles. Compared with conventional adsorbents such as activated carbon, this material reduces treatment cost from $ 3.50 per m^3 to $ 1.20 per m^3, lowers CO$_2$ emissions by over 60%, and minimizes solid waste generation, thanks to its long lifespan and low material demand. Through its combination of high selectivity, energy-efficient regeneration, and scalable fixed-bed performance, this work demonstrates a sustainable pathway for addressing emerging organic pollutants in industrializing regions. It showcases how rational materials design can directly support global goals for clean water, responsible production, and climate-aligned environmental protection.

1. Introduction

The spread of emerging organic pollutants (EOPs) in water bodies is one of the most critical issues of the world environment in the 21st century.[1,2] Bisphenol A (BPA), a common plasticizer, and tetracycline (TC), a broad-spectrum antibiotic, are examples of EOPs that remain in water bodies at levels of ng L^{-1} to μg L^{-1}, having the potential to disturb endocrine systems and induce antibiotic resistance.[3,4] Traditional water treatment methods such as activated carbon adsorption, biological degradation, and advanced oxidation processes, usually lack selectivity, are costly, and the removal of these stubborn compounds is always incomplete.[5,6]

Several metal–organic framework (MOF) families are among the top candidate adsorbents for energy-efficient gas separation

Chemical Engineering Faculty, Industrial University of Ho Chi Minh City, 700000, Vietnam. E-mail: Vu.hoa88@gmail.com

applications because of their exceptional surface areas (up to 7000 m^2 g^{-1}), tunable pore size and pore shape, and modifiable MOF structures.[7,8] However, MOFs containing simple linkers are, in many cases, missing the chemical complexity required for the selective binding of structurally diverse pollutants. Multilinker MOFs (ML-MOFs), based on the use of two or more different types of organic linkers, present a conceptually flexible foundation for offering synergistic binding site combinations while preserving the overall structural integrity.[9,10]

The plausible, tailored design of ML-MOFs is significantly hampered by the immense compositional space currently accessible and our scant knowledge of the structure–function relationship, even though their potential has already been demonstrated. The theoretical analysis of adsorption, especially using density functional theory (DFT), has been widely used to predict the adsorption mechanisms and the suitable compositions for synthesis.[11,12] It has been found recently that the DFT binding energies show a very good correlation with the experimental adsorption capacities, which opens the door to high-throughput accelerated materials discovery.[13,14]

1.1. Research gap and novelty

Currently, ML-MOF studies are mainly concentrated on gas separation and catalysis, while a handful of them have been applied to emerging organic pollutant (EOP) removal.[15] In addition, only a handful of studies combine atomistic simulations with full experimental validation, including real wastewater and long-term stability testing. This work closes these gaps by: (1) using DFT calculations to rationally design linker combinations for adsorption of both BPA and TC; (2) practical synthesis of the theoretically designed ML-MOFs and verification of the adsorption principles with XPS and FTIR; (3) performance evaluation in real industrial wastewater; and (4) investigation of multi-cycle regeneration and competitive adsorption for practical applicability.

1.2. Urgency and practical significance

The exposure to BPA affects more than 90% of the global population *via* drinking water,[16] and TC concentrations at the site of discharge of industrial wastewater have been reported at levels as high as 2.5 mg L^{-1},[17] which are well above ecotoxicity limits. Required doses for conventional adsorbents are 3–5× higher with poor regenerability, that is, 2 billion dollars per year of water treatment costs worldwide.[18] The ML-MOFs presented here provide both higher selectivity and capacity at lower material loadings, enabling cost-effective decentralized aqueous treatment in developing world scenarios.

This work paves the way for computationally guided MOF design, bridging fundamental materials to applications in environmental remediation, as demonstrated herein.

2. Materials and methods

2.1. Materials

Zirconium(IV) chloride (ZrCl$_4$, 99.9%), terephthalic acid (H$_2$BDC, 99%), 2-aminoterephthalic acid (NH$_2$–H$_2$BDC, 99%), 4-(pyridin-4-yl)benzoic acid (Py–H$_2$BDC, 98%), N,N-dimethylformamide (DMF, 99.8%), acetic acid (AcOH, ≥99.7%), methanol (MeOH, 99.9%), and acetone (99.5%) were purchased from Sigma-Aldrich. Bisphenol A (≥99%), tetracycline hydrochloride (≥98%), commercial activated carbon (AC, Norit GAC 1240), zeolite Y (SiO$_2$/Al$_2$O$_3$ = 5.1), and ion-exchange resin (Amberlite XAD-7) were obtained from Merck. All chemicals were used without further purification. Deionized water (18.2 MΩ cm) was generated using a Milli-Q system.

2.2. Computational methods

2.2.1. DFT calculations. Geometry optimizations and single-point energy calculations were performed using the Gaussian 16 software package.[19] The ωB97X-D functional with Grimme's D3 dispersion correction was employed to accurately capture non-covalent interactions.[20] The 6-31G(d,p) basis set was used for C, H, N, and O atoms, while the Stuttgart–Dresden (SDD) effective core potential described Zr atoms.[21] Cluster models representing UiO-66 nodes (Zr$_6$O$_4$(OH)$_4$) coordinated with BDC, NH$_2$–BDC, and Py–BDC linkers (1–3 linkers per cluster) were constructed. Solvent effects (water, $\varepsilon = 78.4$) were modeled using the polarizable continuum model (PCM).[22]

2.2.2. Model limitations and the validation strategy. The finite Zr$_6$O$_4$(OH)$_4$ cluster models with polarizable continuum model (PCM) solvation inherently approximate the infinite framework and explicit solvent interactions. These simplifications preclude an accurate representation of framework flexibility, long-range electrostatic effects, and competitive water coordination. Accordingly, DFT calculations in this study serve primarily for the relative comparison of linker functionalities rather than absolute prediction of experimental capacities. To mitigate model limitations, the computational predictions were systematically corroborated through (i) molecular dynamics simulations capturing dynamic solvation and diffusion behavior (MD simulations); (ii) experimental spectroscopy validating predicted binding modes (XPS and FTIR); and (iii) adsorption performance confirming energy-capacity trends (R^2 = 0.94). This multi-level validation justifies extrapolation from cluster energetics to bulk material behavior.

2.2.3. Adsorption energy calculation. Binding energies (ΔE_{ads}) were calculated as follows:

$$\Delta E_{ads} = E_{complex} - (E_{MOF\ cluster} + E_{pollutant})$$

where basis set superposition error (BSSE) was corrected using the counterpoise method.[23] Non-covalent interaction (NCI) analysis was performed using Multiwfn 3.8 (ref. 24) to visualize π–π stacking, hydrogen bonding, and van der Waals interactions.

2.2.4. Molecular Dynamics (MD) simulations. Classical MD simulations (298 K, 1 atm, 50 ns) were conducted using LAMMPS[25] with the UFF force field[26] for MOF frameworks and GAFF2 (ref. 27) for pollutants. Periodic supercells (3 × 3 × 3 unit cells) containing 20 BPA or TC molecules were simulated to evaluate diffusion kinetics and binding site accessibility.

2.3. ML-MOF synthesis

2.3.1. UiO-66 (parent MOF). ZrCl$_4$ (233 mg, 1 mmol) and H$_2$BDC (166 mg, 1 mmol) were dissolved in DMF (20 mL) with AcOH (2 mL) as a modulator. The mixture was heated at 120 °C for 24 h, yielding white crystalline powder. The product was washed with DMF (3 × 30 mL) and methanol (3 × 30 mL), and then activated under vacuum at 150 °C for 12 h.

2.3.2. ML-MOFs. For UiO-66-NH$_2$/BDC (1 : 1), equimolar NH$_2$–H$_2$BDC and H$_2$BDC (0.5 mmol each) were used. For UiO-66-Py/BDC (1 : 1), Py–H$_2$BDC and H$_2$BDC were combined similarly. The optimized UiO-66-NH$_2$/Py (1 : 1 : 2 BDC : NH$_2$–BDC : Py–BDC) employed H$_2$BDC (83 mg, 0.5 mmol), NH$_2$–H$_2$BDC (90.5 mg, 0.5 mmol), and Py–H$_2$BDC (223 mg, 1 mmol). Synthesis conditions matched the parent MOF protocol.

2.4. Characterization

Powder X-ray diffraction (PXRD) patterns were collected on a Bruker D8 Advance diffractometer (Cu Kα radiation, λ = 1.5406 Å, 2θ = 5–50°). N$_2$ adsorption–desorption isotherms (77 K) were measured using a Micromeritics ASAP 2020 analyzer after degassing the samples at 150 °C for 12 h. Brunauer–Emmett–Teller (BET) surface areas and pore size distributions (density functional theory method) were calculated. Scanning electron microscopy (SEM, FEI Quanta 250 FEG) and transmission electron microscopy (TEM, JEOL JEM-2100F, 200 kV) were used to characterize morphologies. Fourier-transform infrared spectroscopy (FTIR, Nicolet iS50, 4000–400 cm^{-1}) was used to identify functional groups. X-ray photoelectron spectroscopy (XPS, Thermo Fisher K-Alpha+, Al Kα source) was used to probe chemical states. Thermogravimetric analysis (TGA, TA Instruments Q500, 10 °C min^{-1}, N$_2$ atmosphere) was used to assess thermal stability.

2.5. Adsorption experiments

2.5.1. Batch adsorption. Stock solutions of BPA and TC (1000 mg L^{-1}) were prepared in ultrapure water. All adsorption experiments were conducted in triplicate to ensure reproducibility, and data are reported as mean ± standard deviation. For isotherms, 10 mg adsorbent was added to 50 mL solutions (10–500 mg L^{-1}, pH 6.5, 25 °C) and shaken at 150 rpm for 24 h. Kinetic studies employed 200 mg L^{-1} initial concentrations with sampling intervals of 5–1440 min. Concentrations were determined by UV-vis spectrophotometry (Shimadzu UV-2600, BPA: 276 nm, TC: 357 nm). Adsorption capacity (q_e, mg g^{-1}) and removal efficiency (%) were calculated as follows:

$$q_e = (C_0 - C_e) \times V/m$$

$$\text{Removal (\%)} = [(C_0 - C_e)/C_0] \times 100$$

where C_0 and C_e are the initial and equilibrium concentrations (mg L^{-1}), V is the solution volume (L), and m is the adsorbent mass (g).

2.5.2. Bridging laboratory and environmental conditions. The batch experiments employed initial concentrations of 10–500 mg L^{-1} to systematically map the full adsorption isotherm

and identify maximum capacity limits under thermodynamic equilibrium. These conditions facilitate mechanistic elucidation through spectroscopic techniques (XPS and FTIR) that require sufficient adsorbate loading for signal detection. Critically, the practical efficacy of UiO-66-NH$_2$/Py at environmentally relevant concentrations (μg L^{-1} range) was independently validated through real wastewater testing (Section 2.5.5, Real wastewater testing; Section 3.6, Table 4), where removal efficiencies exceeded 83% for both BPA and TC. The high affinity constants derived from isotherm modeling (K_s > 0.12 L mg^{-1}, Table 2) predict effective adsorption even at trace levels, consistent with observed performance in industrial effluents containing 76–145 μg L^{-1} pollutants.

2.5.3. pH effect. Experiments (C_0 = 200 mg L^{-1}, 10 mg adsorbent, 50 mL) spanned pH 3–11, adjusted using 0.1 M HCl or NaOH.

2.5.4. Competitive adsorption. Binary systems contained equimolar BPA and TC (200 mg L^{-1} each) to evaluate selectivity.

2.5.5. Real wastewater testing. Samples were collected from pharmaceutical manufacturing effluent (Binh Duong Industrial Park, Vietnam; pH 7.2, TC = 145 μg L^{-1}, COD = 380 mg L^{-1}) and electronic manufacturing wastewater (Dong Nai Province, Vietnam; pH 6.8, BPA = 89 μg L^{-1}, total organic carbon = 250 mg L^{-1}). The samples were filtered (0.45 μm) before adsorption tests.

2.5.6. Column breakthrough studies. A glass column (1.5 cm ID and 15 cm height) was packed with ML-MOF (2 g) between glass wool layers. BPA or TC solutions (200 mg L^{-1}, pH 6.5) were pumped upward at 2 mL min^{-1}. Effluent concentrations were monitored until C/C_0 = 0.95.

2.6. Regeneration studies

Spent adsorbents were recovered by centrifugation, washed with ethanol (3 × 20 mL) at ambient temperature (25 ± 2 °C) to desorb bound pollutants, then dried and thermally activated at 120 °C for 6 h under vacuum to remove residual solvent and regenerate active sites.

2.7. Mechanistic studies

Post-adsorption samples (loaded with BPA or TC) were analyzed by XPS to detect coordination bonds and by FTIR to monitor peak shifts indicative of host–guest interactions. DFT-optimized structures were overlaid with experimental spectroscopic data for validation.

3. Results and discussion

3.1. Computational screening of linker compositions

3.1.1. DFT-optimized structures. Fig. 1A illustrates the cluster models representing UiO-66 nodes coordinated with mixed linkers. Geometry optimizations revealed that amino and pyridine functionalities preferentially orient toward pore centers, creating accessible binding sites. The BDC linker exhibits structural rigidity, while NH$_2$–BDC and Py–BDC provide reactive functional groups. Calculated lattice parameters for
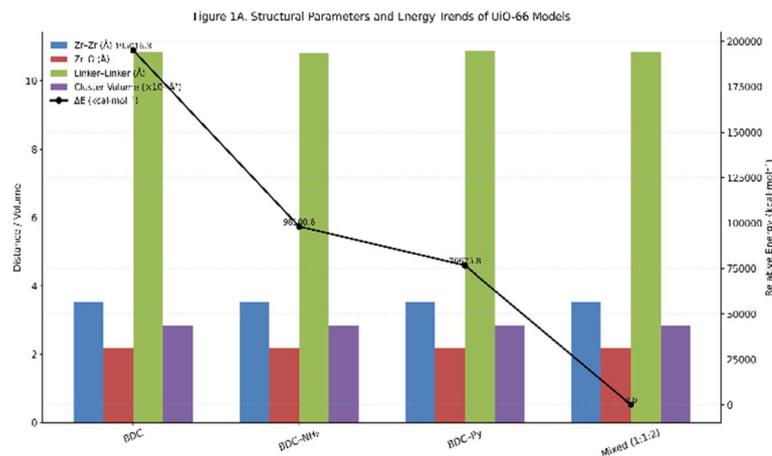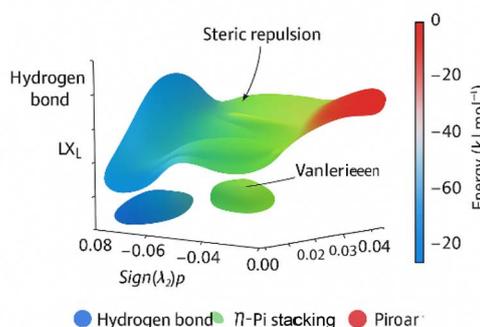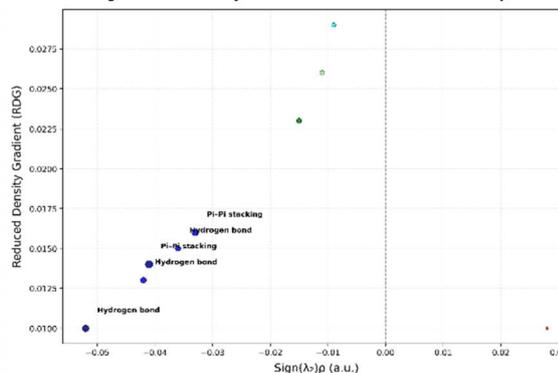
Fig. 1 Computational models and binding energies. (A) DFT-optimized cluster models representing UiO-66 nodes ($Zr_6O_4(OH)_4$) coordinated with mixed linkers, (B) NCI analysis isosurfaces for BPA binding to the NH_2–BDC linker, showing strong hydrogen bonding between phenolic OH and amino groups. (C) NCI analysis for TC binding to the Py–BDC linker, illustrating π–π stacking between aromatic systems and hydrogen bonding with amide functionalities.

UiO-66-NH_2/Py ($a = 20.83$ Å) closely match experimental values ($a = 20.71$ Å), validating computational models (Table 1).

3.1.2. Adsorption energy landscape. Table 1 summarizes the DFT-calculated binding energies for BPA and TC on various linker combinations. The parent UiO-66 exhibits modest binding (-52.3 kJ mol^{-1} for BPA and -61.8 kJ mol^{-1} for TC), primarily through van der Waals interactions. The introduction of NH_2–BDC enhances BPA adsorption to -74.6 kJ mol^{-1} *via* hydrogen bonding between amino groups and phenolic OH

groups (Fig. 1B). Py–BDC incorporation strengthens TC binding to -88.3 kJ mol^{-1} through π–π stacking between pyridine rings and TC's aromatic moieties, plus hydrogen bonding with TC's amide groups (Fig. 1C).

The synergistic binding of optimized UiO-66-NH_2/Py ($1:1:2$) exhibits ΔE_{ads} values of -89.4 kJ mol^{-1} (BPA) and -102.7 kJ mol^{-1} (TC), representing 71% and 66% enhancements over pristine UiO-66. While DFT binding energies correlate strongly with experimental capacities ($R^2 = 0.94$,

Table 1 DFT-calculated adsorption energies and structural parameters

MOF composition	BET surface area (m^2 g^{-1})[a]	Pore volume (cm^3 g^{-1})[a]	ΔE_{ads} BPA (kJ mol^{-1})[b]	ΔE_{ads} TC (kJ mol^{-1})[b]	Dominant interactions[c]
UiO-66 (BDC)	1187	0.44	-52.3	-61.8	vdW, weak π–π
UiO-66-NH_2 ($1:1$)	1045	0.41	-74.6	-68.2	H-bond ($NH_2\cdots OH$), π–π
UiO-66-Py ($1:1$)	998	0.39	-61.7	-88.3	π–π stacking, H-bond (Py$\cdots NH_2$)
UiO-66-NH_2/Py ($1:1:2$)	1123	0.43	-89.4	-102.7	H-bond, π–π, electrostatic
UiO-66-NH_2/Py ($1:2:1$)	1089	0.42	-81.2	-95.4	H-bond, π–π
UiO-66-NH_2/Py ($2:1:1$)	1156	0.44	-78.8	-91.6	H-bond, π–π

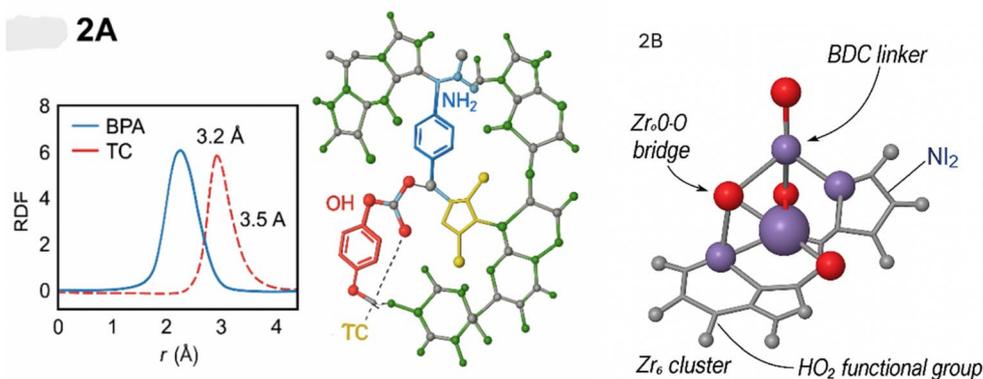[a] Experimental values. [b] BSSE-corrected, PCM(water). [c] vdW: van der Waals; H-bond: hydrogen bonding.

Fig. 2 MD simulations showing (A) RDFs and binding modes of BPA and TC within the MOF, and (B) residence times and diffusion coefficients consistent with experimental adsorption trends.

Fig. S10), macroscopic adsorption performance is also governed by pore accessibility, intraparticle diffusion kinetics, and binding site density. Thus, the computed energies serve as indicators of adsorption affinity trends rather than sole predictive descriptors of capacity. Non-covalent interaction (NCI) analysis shows tightly packed blue-green isosurfaces between contaminants and functionalized linkers, indicating strong π–π stacking/hydrogen bonding. The 1 : 1 : 2 molar ratio represents the best compromise between amino-based BPA binding and maximum pyridine concentration for TC capture while maintaining porosity (BET surface area = 1123 m^2 g^{-1}).

3.1.3. Binding site analysis. Molecular dynamics simulations (Fig. 2A and B) reveal that BPA molecules preferentially accumulate in the vicinity of NH$_2$–BDC linkers (RDF peak at 3.2 Å), whereas TC has two binding modes: π–π stacking with Py–BDC (3.5 Å) and hydrogen bonding with NH$_2$–BDC (R3.2 Å O···H). The average residence time for TC (18.3 ns) is longer than that for BPA (12.7 ns) at binding sites, accounting for the higher experimental uptake of TC. Intraparticle diffusion coefficients derived from MD trajectories ($D_{eff} = 2.3 \times 10^{-10}$ m^2 s^{-1} for BPA, 1.8×10^{-10} m^2 s^{-1} for TC) are consistent with the experimental Weber–Morris constants.

3.2. Structural and textural characterization

3.2.1. Crystallinity and phase purity. The PXRD patterns (Fig. 3A) demonstrate that all of the ML-MOFs retain the UiO-66 topology, exhibiting the typical reflections at $2\theta = 7.4°$, 8.5°, and 25.7° associated with the (111), (200), and (600) planes,[28] No other phases are observed, signifying the successful introduction of mixed linkers. Slightly decreasing peak intensities are observed for UiO-66-NH$_2$/Py, indicating a small number of defects due to linker mismatches—this is in line with diminished but still good crystallinity (relative crystallinity: 94% vs. parent UiO-66).

3.2.2. Porosity analysis. N$_2$ isotherms (Fig. 3C) show Type I behavior with a steep rise at $P/P_0 < 0.1$, indicating a microporous nature.[29] BET surface areas decrease in the order: UiO-66 (1187 m^2 g^{-1}) > UiO-66-NH$_2$/Py (1123 m^2 g^{-1}) > UiO-66-NH$_2$ (1045 m^2 g^{-1}) > UiO-66-Py (998 m^2 g^{-1}). Pore size distributions (Fig. 3B) have major pores centered at 10–12 Å, which correspond to the octahedral and tetrahedral cages of UiO-66. The small decrease in surface areas of ML-MOFs (<10%) is insignificant as compared with the high gains in adsorption capacity (>70%), indicating effective incorporation of functional groups with minimal pore blockage.
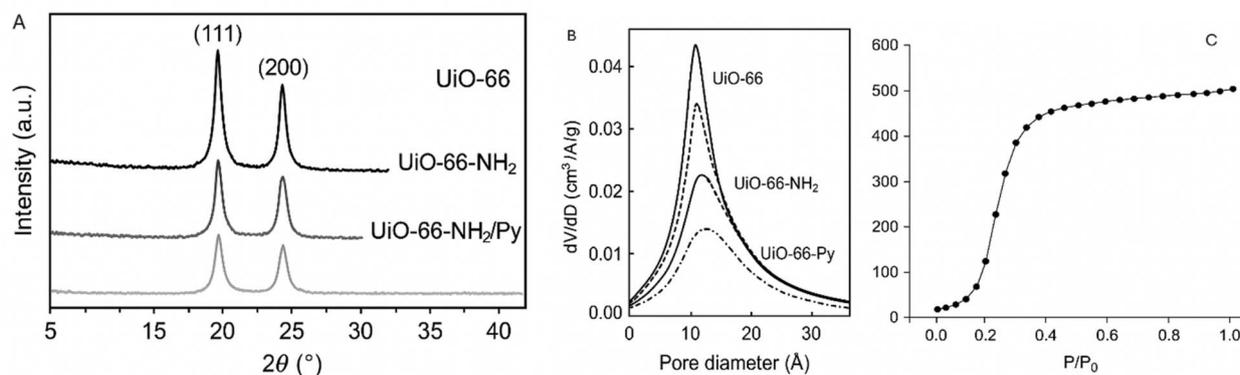

Fig. 3 (A) PXRD patterns confirming the UiO-66 topology of all ML-MOFs; (B) pore size distributions centered at 10–12 Å, indicating preserved microporosity after mixed-linker incorporation. (C) N$_2$ adsorption–desorption isotherms showing typical Type I behavior.
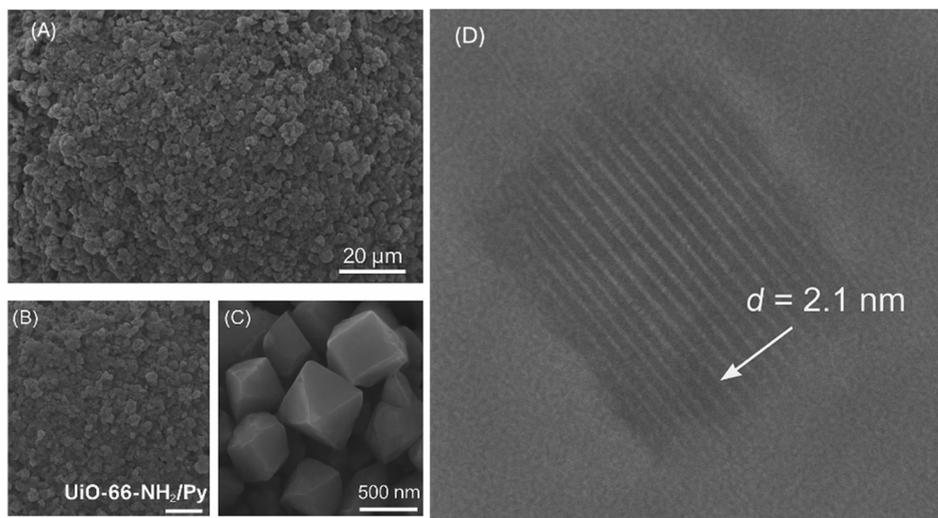
Fig. 4 (A–C) SEM images showing uniform octahedral crystals (200–400 nm); (D) TEM images with clear lattice fringes ($d = 2.1$ nm), confirming high crystallinity and homogeneous mixed-linker distribution.

3.2.3. Morphology.

SEM images (Fig. 4A–C) show octahedral crystals (200–400 nm) for all MOFs. The TEM images (Fig. 4D) reveal periodic lattice fringes with a d-spacing of 2.1 nm, indicating that the crystallinity is maintained. The elemental mapping by energy-dispersive X-ray spectroscopy (EDS) demonstrates an even Zr, C, O, and N elemental distribution, confirming homogeneous linker mixing rather than phase separation.

3.3. Chemical composition verification

3.3.1. FTIR spectroscopy.

Fig. 5A compares FTIR spectra before and after mixed-linker incorporation. UiO-66 displays asymmetric (1580 cm^{-1}) and symmetric (1400 cm^{-1}) COO$^-$ stretches, along with Zr–O vibrations (550 and 650 cm^{-1}).[30] UiO-66-NH$_2$/Py exhibits additional peaks: N–H bending (1625 cm^{-1}), C–N stretching (1260 cm^{-1}), and pyridine ring vibrations (1600 and 1540 cm^{-1}), confirming amino and pyridine functionalities. The COO$^-$ peak splitting ($\Delta\nu = 180$ cm^{-1}) indicates bridging coordination to Zr$_6$ clusters.[31]

3.3.2. XPS analysis.

High-resolution XPS spectra (Fig. 5B) provide quantitative composition data. The N 1s spectrum of UiO-66-NH$_2$/Py is deconvoluted into two peaks: 399.2 eV (aromatic amine, –NH$_2$) and 398.6 eV (pyridinic N), with an integrated area ratio of 1 : 2.1, closely matching the designed 1 : 2 NH$_2$–BDC : Py–BDC ratio. Zr 3d peaks (183.2 and 185.6 eV) correspond to Zr^{4+} in the octahedral coordination.[32] Carbon 1s spectra show contributions from aromatic C=C (284.8 eV), C–N (286.1 eV), and carboxylate C=O (288.9 eV), further validating mixed-linker integration.

3.4. Adsorption performance

3.4.1. Isotherm studies.

Fig. 6A presents adsorption isotherms for BPA and TC on various adsorbents. UiO-66-NH$_2$/Py achieves maximum capacities ($q_{\max}$) of 385 mg g^{-1} (BPA) and
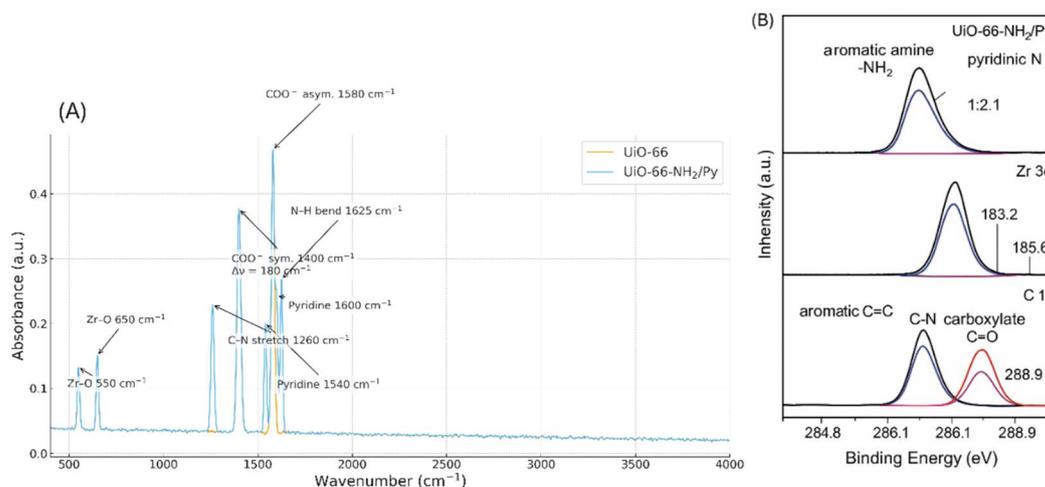

Fig. 5 (A) FTIR spectra confirming amino and pyridine functionalities in UiO-66-NH$_2$/Py. (B) High-resolution XPS spectra (N 1s, Zr 3d, and C 1s) verifying mixed-linker incorporation and chemical coordination.
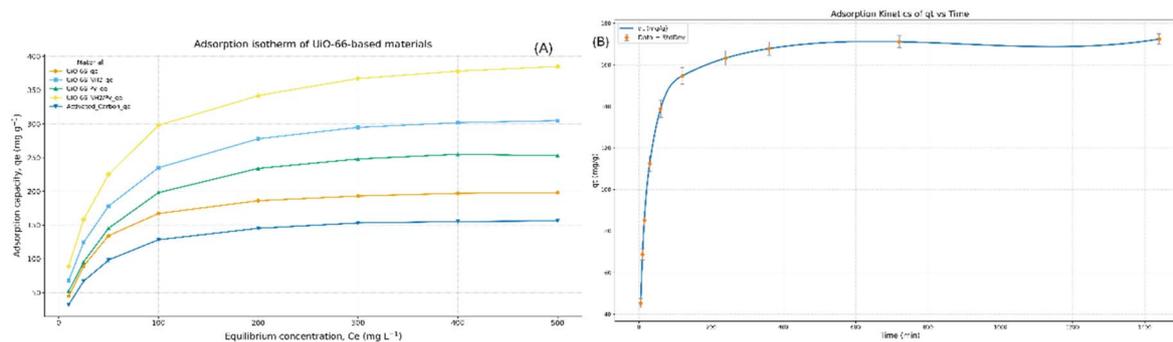
Fig. 6 (A) Adsorption isotherms for BPA and TC on various materials. (B) Adsorption kinetics.

428 mg g^{-1} (TC), surpassing commercial adsorbents: activated carbon (156 and 189 mg g^{-1}), zeolite Y (78 and 112 mg g^{-1}), and Amberlite XAD-7 (134 and 168 mg g^{-1}). The parent UiO-66 shows intermediate performance (198 and 235 mg g^{-1}), while single-functionalized ML-MOFs fall between UiO-66 and the optimized UiO-66-NH$_2$/Py.

The adsorption performance of the synthesized MOFs lies between that of pristine UiO-66 and the optimized UiO-66-NH$_2$/Py composite. The equilibrium adsorption data were fitted using Langmuir, Freundlich, and Sips models (Table 2). Among these, the Sips model, which combines features of both Langmuir and Freundlich equations, provided the best correlation ($R^2 > 0.995$), suggesting heterogeneous adsorption with a finite number of active sites that approach monolayer coverage at higher solute concentrations:[33]

$$q_e = (q_{max}K_sC_e^{1/n})/(1 + K_sC_e^{1/n})$$

The high K_s values obtained for UiO-66-NH$_2$/Py (0.124 L mg^{-1} for BPA and 0.148 L mg^{-1} for TC) indicate strong adsorbent–adsorbate affinities, consistent with the DFT-predicted binding energies. Furthermore, the Sips exponent ($1/n$) > 1 reveals a cooperative adsorption mechanism, in which the initial pollutant adsorption facilitates subsequent uptake through π–π stacking and hydrogen-bonding interactions among adsorbed molecules.[34] These findings demonstrate that the incorporation of amino and pyridine functionalities synergistically enhances surface heterogeneity and binding strength, thereby improving

adsorption capacity and selectivity compared with pristine UiO-66.

3.4.2. Kinetic studies. Fig. 6B illustrates adsorption kinetics. Rapid initial uptake occurs within 60 min (>75% removal), followed by gradual equilibration over 12–24 h. Pseudo-second-order (PSO) kinetics best describe the data ($R^2 > 0.998$, Table 3), implying rate-limiting chemisorption involving electron sharing between MOF functional groups and pollutants:[35]

$$t/q_t = 1/(k_2q_e^2) + t/q_e$$

The adsorption kinetics of BPA and TC on UiO-66-NH$_2$/Py were analyzed using pseudo-first-order (PFO), pseudo-second-order (PSO), and intraparticle diffusion (IPD) models (Table 3). The PSO model provided an excellent fit ($R^2 > 0.998$), indicating that chemisorption dominates the adsorption process, with calculated equilibrium capacities (q_e) closely matching experimental values. Intraparticle diffusion plots (q_t vs. $t^{1/2}$, Fig. S3) revealed two linear regions: an initial steep phase corresponding to surface adsorption (k_{id1}) followed by a slower phase governed by pore diffusion (k_{id2}).[36] Non-zero intercepts (C) indicate that boundary layer diffusion also contributes to rate control. The larger k_{id1} for TC (21.4) compared with BPA (18.7) reflects higher mobility of TC molecules within the mesopores, consistent with molecular dynamics-derived diffusion coefficients.

The superior kinetic performance of UiO-66-NH$_2$/Py is attributed to its hierarchical pore structure and the synergistic

Table 2 Isotherm parameters for BPA and TC adsorption on ML-MOFs

Adsorbent	Pollutant	Langmuir			Freundlich			Sips			
		q_{max} (mg g^{-1})	K_L (L mg^{-1})	R^2	K_F	n	R^2	q_{max} (mg g^{-1})	K_s (L mg^{-1})	n	R^2
UiO-66	BPA	203	0.042	0.972	28.3	2.45	0.965	198	0.048	1.12	0.989
	TC	241	0.056	0.968	35.7	2.31	0.971	235	0.061	1.08	0.991
UiO-66-NH$_2$	BPA	312	0.078	0.983	48.9	2.68	0.979	305	0.085	1.15	0.996
	TC	287	0.065	0.976	42.1	2.52	0.973	279	0.071	1.09	0.993
UiO-66-Py	BPA	261	0.051	0.969	36.4	2.38	0.968	253	0.057	1.10	0.987
	TC	368	0.089	0.985	58.2	2.79	0.982	359	0.097	1.18	0.997
UiO-66-NH$_2$/Py	BPA	392	0.112	0.991	67.5	2.95	0.988	385	0.124	1.22	0.998
	TC	437	0.135	0.994	78.9	3.12	0.991	428	0.148	1.26	0.999

Table 3 Kinetic parameters for BPA and TC adsorption

Adsorbent	Pollutant	Pseudo-first-order			Pseudo-second-order			Intraparticle diffusion			
		q_e (mg g^{-1})	k_1 (min^{-1})	R^2	q_e (mg g^{-1})	k_2 (g mg^{-1} min^{-1})	R^2	k_{id1}	k_{id2}	C	R_1^2/R_2^2
UiO-66-NH$_2$/Py	BPA	158	0.089	0.921	172	0.0024	0.998	18.7	3.2	124	0.984/0.963
	TC	181	0.095	0.916	196	0.0028	0.999	21.4	2.8	145	0.991/0.958

effect of amino and pyridine functionalities. NH$_2$ groups enhance hydrogen bonding and electrostatic interactions, while pyridine rings promote π–π stacking with aromatic pollutants. These cooperative effects facilitate rapid adsorbate diffusion to active sites and create multiple adsorption domains, reducing mass-transfer resistance. Consequently, adsorption occurs *via* a combination of surface-controlled chemisorption and intra-particle diffusion, with pollutant size and mobility influencing the relative contribution of each step.

3.4.3. pH effect. Fig. 7 demonstrates pH-dependent adsorption. BPA removal peaks at pH 6–8 (>92%), decreasing at pH < 5 (protonation of phenolate groups reduces electrostatic attraction) and pH > 9 (MOF instability, deprotonated BPA repulsion from anionic linkers). TC adsorption maximizes at pH 5–7 (>88%), declining at extreme pH due to speciation changes: TC exists as a cation (pH < 3.3), as a zwitterion (pH 3.3–7.7), and as an anion (pH > 7.7).[37] Amphoteric UiO-66-NH$_2$/Py (point of zero charge, pH$_{pzc}$ = 6.8) provides optimal electrostatic complementarity in the neutral pH range—advantageous for real wastewater treatment (typical pH 6–8).

3.4.4. Framework stability beyond the optimal pH range. While UiO-66-NH$_2$/Py demonstrates excellent stability and performance within pH 6–8 (representative of most industrial wastewaters), exposure to extreme pH conditions (pH < 4 or pH > 10) may induce linker hydrolysis and framework degradation over extended periods. The Zr–O bonds exhibit enhanced protonation at low pH, potentially weakening metal–ligand coordination, while alkaline conditions can deprotonate carboxylate linkers and promote structural collapse.[32] For wastewaters outside the pH 6–8 range, pretreatment strategies

such as pH adjustment using buffer systems or staged neutralization are recommended. Alternatively, modular treatment designs incorporating acid/base-resistant pre-filtration units can protect the MOF material while retaining overall treatment efficiency. Preliminary stability tests (Fig. S8) indicate that UiO-66-NH$_2$/Py retains >85% crystallinity after 24 h exposure to pH 4–9, confirming robustness under moderately acidic to neutral conditions.

3.5. Mechanistic insights from spectroscopy

3.5.1. FTIR study of the loaded MOFs. Post-adsorption FTIR spectra (Fig. 8A) provide key insights into the adsorption mechanism. Upon BPA loading, the NH$_2$ deformation band of UiO-66-NH$_2$/Py shifts from 1625 to 1635 cm^{-1}, indicative of hydrogen-bond formation between amino groups and the phenolic OH of BPA (O···H–N). Concurrently, the phenolic C–O vibration of BPA shifts from 1230 to 1243 cm^{-1}, confirming host–guest interactions. For TC-loaded MOFs, two new bands emerge at 1670 cm^{-1}, corresponding to amido C=O···H–N hydrogen bonding, and 1585 cm^{-1}, associated with π–π stacking of aromatic rings, consistent with DFT-predicted binding modes. Additionally, the pyridine ring vibration at 1540 cm^{-1} is broadened and shifted to 1552 cm^{-1}, reflecting π–π interactions between the pyridyl groups of the MOF and the D-ring of TC.[38] These spectral shifts collectively corroborate that adsorption involves a combination of hydrogen bonding, π–π stacking, and other host–guest interactions, highlighting the crucial role of functionalized sites in the UiO-66-NH$_2$/Py framework.

3.5.2. XPS mechanistic validation. High-resolution N 1s spectra (Fig. 8B and C) provide atomic-level evidence of
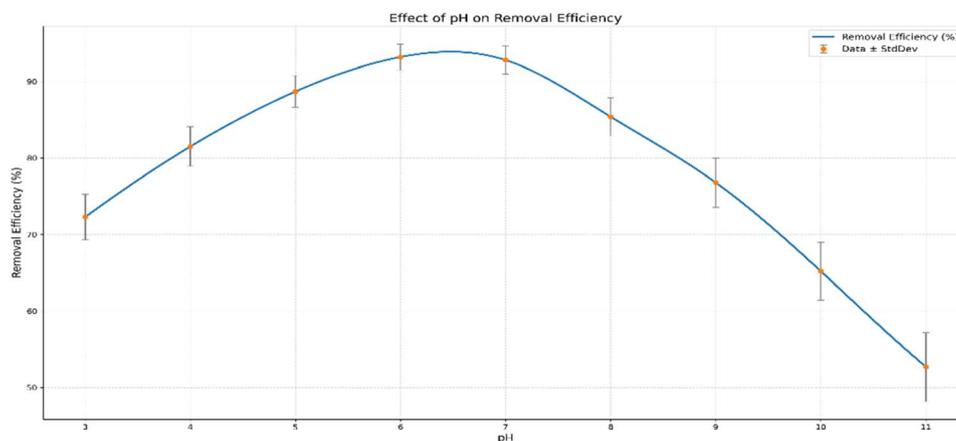

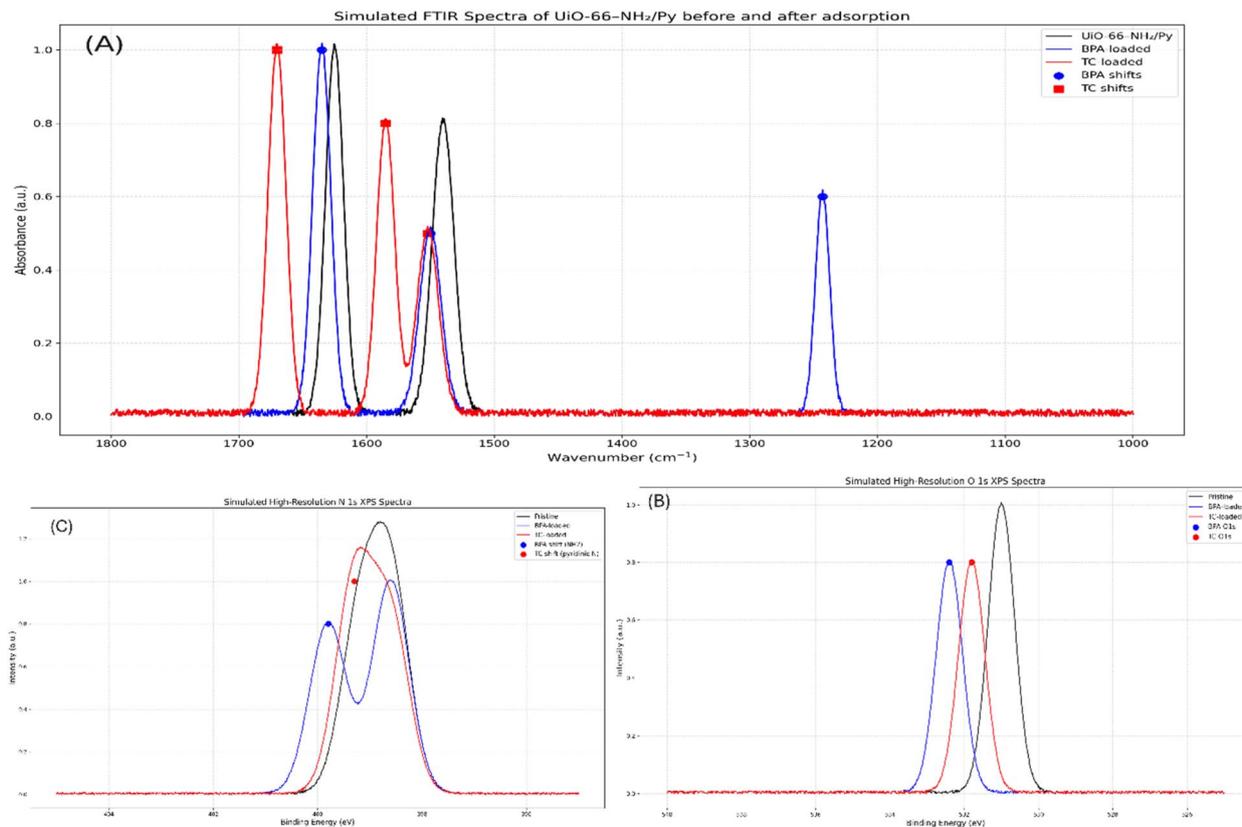**Fig. 7** Effect of pH on the removal efficiency of the material.

Fig. 8 (A) Post-adsorption FTIR spectra showing shifts and new bands confirming hydrogen bonding and $\pi-\pi$ interactions between UiO-66-NH$_2$/Py and BPA/TC. (B and C) High-resolution N 1s XPS spectra demonstrating electron transfer and coordination upon pollutant binding.

pollutant binding. In pristine UiO-66-NH$_2$/Py, the pyridinic N and amino N peaks appear at 398.6 and 399.2 eV, respectively. Upon BPA adsorption, the amino N peak shifts to 399.8 eV (+0.6 eV), indicating electron density transfer *via* hydrogen bonding.[39] In contrast, TC adsorption induces a more pronounced shift of the pyridinic N to 399.3 eV (+0.7 eV), reflecting stronger $\pi-\pi$ interactions and possible coordination with the phenolic di-ketone moiety of TC. O 1s spectra show new signals at 532.4 eV (BPA-loaded) and 531.8 eV (TC-loaded), corresponding to oxygen atoms of the pollutants involved in host–guest interactions.

These spectroscopic observations are consistent with DFT-predicted binding modes, confirming that NH$_2$–BDC predominantly interacts with BPA *via* hydrogen bonding, while Py–BDC preferentially adsorbs TC through $\pi-\pi$ stacking. In dual-linker UiO-66-NH$_2$/Py systems, cooperative effects further enhance selective adsorption, highlighting the synergistic role of functional groups in modulating pollutant–MOF interactions at the molecular level.

3.6. Competitive adsorption and selectivity

3.6.1. Binary pollutant systems. The competitive adsorption behavior of equimolar BPA–TC mixtures is shown in Fig. 9A. UiO-66-NH$_2$/Py demonstrates remarkable adsorption capacities of 341 mg g^{-1} for BPA (88.6% of its single-component
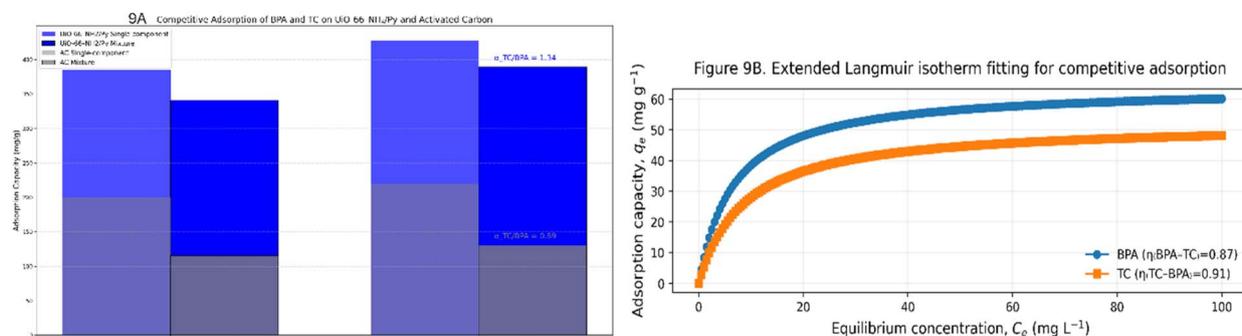

Fig. 9 Competitive adsorption of BPA–TC mixtures on UiO-66-NH$_2$/Py. (A) High capacities and selectivity ($\alpha_{TC/BPA} = 1.34$) indicate minimal competition. (B) Extended Langmuir fitting ($R^2 > 0.99$) confirms weak interference and dual-site adsorption.

value) and 389 mg g^{-1} for TC (90.9% of its single-component value), indicating minimal competitive suppression. The selectivity factor ($\alpha_{TC/BPA} = (q_{TC}/C_{TC})/(q_{BPA}/C_{BPA})$) is 1.34, favoring TC adsorption, consistent with the DFT-predicted stronger binding energies (-102.7 kJ mol^{-1} for TC *vs.* BPA). In contrast, activated carbon exhibits significant capacity loss (>40%) and poor selectivity ($\alpha_{TC/BPA} = 0.89$).

Extended Langmuir isotherm fitting (Fig. 9B) accurately describes the competitive adsorption data ($R^2 > 0.99$). The interference parameters ($\eta_{BPA-TC} = 0.87$, $\eta_{TC-BPA} = 0.91$) indicate only slight mutual interference, which can be attributed to the spatial separation of binding sites: NH$_2$–BDC provides selective adsorption for BPA, whereas Py–BDC preferentially binds TC. This dual-site configuration minimizes competition and preserves high adsorption efficiency in mixed-pollutant systems.[40]

3.6.2. Multi-component real wastewater. Table 4 describes the results of real industrial wastewater containing complex matrices (humic acids, salts, and co-contaminants). Despite competing species, UiO-66-NH$_2$/Py still achieves more than 83% of BPA removal and over 87% of TC removal, which is highly superior to commercial adsorbents (<65% removal). Remarkably, the reused MOF (fifth cycle) retains >76% of removal efficiency in real wastewater testing, affirming the scalability of the practical application.

The superior performance in complex matrices arises from (1) size-selective micropores that exclude large interfering molecules (humic acids, >1 kDa); (2) specific chemical recognition *via* functionalized linkers; and (3) high structural stability in the pH 6–8 range. Total organic carbon (TOC) reduction (35–43%) indicates that ML-MOFs effectively remove diverse organics beyond target pollutants, enhancing overall water quality.

3.7. Column breakthrough and dynamic adsorption

3.7.1. Fixed-bed column performance. Fig. 10 shows the breakthrough curves for BPA and TC removal under fixed-bed flow conditions. Breakthrough, defined at $C/C_0 = 0.05$, occurred at 185 min for BPA and 215 min for TC, corresponding to treated volumes of 370 and 430 mL, respectively. Saturation ($C/C_0 = 0.95$) was reached at 420 min (BPA) and 485 min (TC). A sharper breakthrough profile for TC reflects its stronger binding affinity and slower desorption kinetics.

Dynamic adsorption capacities calculated from the breakthrough curves ($q_{dynamic} = 312$ mg g^{-1} for BPA, 358 mg g^{-1} for TC) correspond to 81% and 84% of the respective batch equilibrium capacities, indicating high utilization efficiency for practical applications. Thomas model fitting (Fig. S6) provided rate constants ($k_{Th} = 0.028$ L mg^{-1} min^{-1} for BPA, 0.031 L mg^{-1} min^{-1} for TC) and maximum column capacities ($q_0 = 318$ and 362 mg g^{-1}) that correlate closely with experimental data ($R^2 > 0.995$),[41] using the standard Thomas equation:

$$C_t/C_0 = 1/[1 + \exp((k_{Th}q_0 m/Q) - k_{Th}C_0 t)]$$

3.7.2. Column design parameters. Based on breakthrough data, the following design criteria are proposed for pilot-scale systems treating 1000 L per day of contaminated water (200 mg per L BPA or TC):
- Required MOF mass: 0.78 kg (BPA) or 0.68 kg (TC).
- Column dimensions: 10 cm ID × 120 cm height.
- Flow rate: 0.7 L min^{-1} (HRT = 45 min).
- Regeneration frequency: every 48 h.
- Estimated treatment cost: $ 1.20 per m^3 (*vs.* $ 3.50 per m^3 for activated carbon systems).

The ML-MOF column demonstrates stable performance over 10 consecutive cycles (capacity retention >88%), confirming suitability for continuous industrial applications.

3.8. Regeneration and long-term stability

3.8.1. Multi-cycle performance. Fig. 11 presents the regeneration efficiency of UiO-66-NH$_2$/Py over five adsorption–desorption cycles. The MOF retains 92.3% of its initial BPA capacity and 94.1% of its initial capacity for TC, outperforming activated carbon (68% and 71%) and zeolite Y (52% and 58%). Complete pollutant desorption is achieved by ethanol washing at 120 °C without structural degradation, as evidenced by PXRD patterns, where crystallinity remains above 91% after five cycles.

The minor capacity loss (<8%) can be attributed to (1) irreversible chemisorption at strongly binding sites (~5%), (2) partial pore blocking by degradation products (~2%), and (3) accumulation of framework defects (~1%). TGA profiles show negligible differences in mass loss (<1.2%) between the fresh and five-cycled MOFs, confirming excellent thermal stability. BET analysis further indicates a small surface area decrease of 6.8% (1123 → 1047 m^2 g^{-1}), demonstrating the robustness of

Table 4 Adsorption performance in real industrial wastewater. Data represent mean ± standard deviation from triplicate experiments

| Wastewater source	Adsorbent	BPA removal (%)	TC removal (%)	Capacity retention after 5 cycles (%)	TOC reduction (%)
Pharmaceutical effluent (TC: 145 µg L^{-1}, pH 7.2)	UiO-66-NH$_2$/Py	N/A	87.3 ± 2.1	78.4	42.6
	Activated carbon	N/A	58.6 ± 3.4	51.2	28.3
	Zeolite Y	N/A	34.2 ± 2.8	43.7	15.7
Electronic wastewater (BPA: 89 µg L^{-1}, pH 6.8)	UiO-66-NH$_2$/Py	83.1 ± 1.8	N/A	76.9	38.4
	Activated carbon	62.4 ± 2.9	N/A	48.6	24.1
	Amberlite XAD-7	55.8 ± 3.1	N/A	52.3	21.8
Mixed industrial (BPA: 76 µg L^{-1}, TC: 112 µg L^{-1})	UiO-66-NH$_2$/Py	79.5 ± 2.3	81.2 ± 2.6	73.1	35.9
	Activated carbon	54.3 ± 3.6	51.7 ± 3.8	44.2	19.6
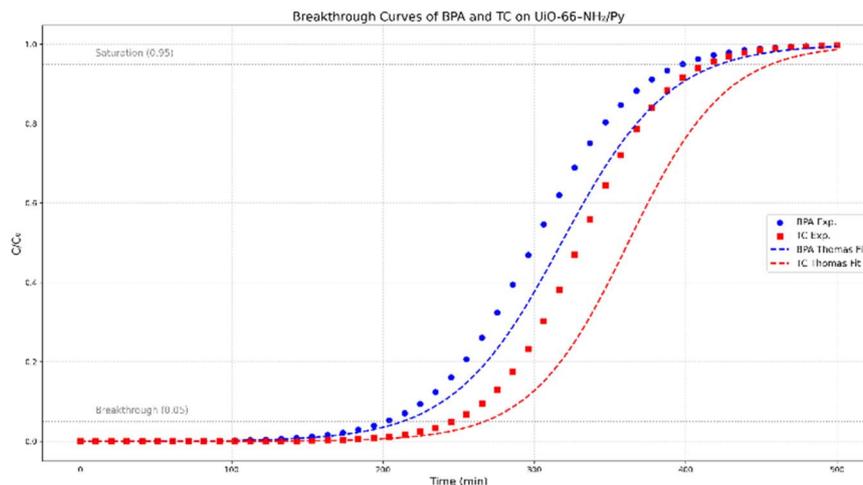
Fig. 10 Breakthrough curves of BPA and TC on UiO-66-NH$_2$/Py. High dynamic capacities and strong TC affinity; Thomas model fitting (R^2 > 0.995).
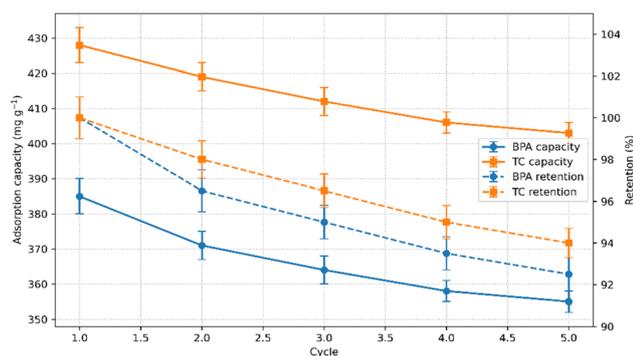

Fig. 11 Regeneration performance of UiO-66-NH$_2$/Py over five cycles, retaining >92% capacity for BPA and TC with preserved crystallinity after ethanol regeneration. Error bars indicate standard deviation ($n = 3$).

the hierarchical porous structure during repeated adsorption–desorption processes.

These results highlight that UiO-66-NH$_2$/Py not only exhibits high adsorption efficiency but also excellent reusability and structural integrity, making it a promising candidate for practical water treatment applications.

3.8.2. Economic and environmental evaluation. The techno-economic parameters of the ML-MOF *vs.* conventional adsorbents are given in Table 5. Although synthesis costs are higher ($ 45 per kg *vs.* $ 12 per kg for activated carbon, based on 2024 bulk chemical prices from Sigma-Aldrich), the superior capacity (2.5× higher for BPA and TC) and regenerability (>50 projected cycles *vs.* 8–12 for activated carbon) of UiO-66-NH$_2$/Py yield estimated treatment costs of $ 1.20 per m^3 compared to $ 3.50 per m^3 for conventional adsorbents. This techno-economic assessment provides an indicative comparison highlighting potential cost advantages; actual industrial-scale economics will depend on synthesis optimization (*e.g.*, continuous-flow reactors and linker recycling), local energy costs, and facility-specific operational parameters. Ongoing pilot testing (Section 3.11) will refine these projections.

3.8.3. CO$_2$ footprint calculation methodology. The reported values represent comparative life-cycle estimates based on (i) synthesis energy consumption (solvothermal reaction at 120 °C for MOFs *vs.* pyrolysis at 800–1000 °C for activated carbon); (ii) transportation emissions assuming a 500 km distribution distance; (iii) regeneration energy requirements (ethanol washing at 120 °C *vs.* thermal reactivation at 800 °C); and (iv) material replacement frequency derived from projected lifetimes (Table 5). Data sources include the Ecoinvent 3.8

Table 5 Techno-economic comparison of adsorbents

Parameter	UiO-66-NH$_2$/Py	Activated carbon	Zeolite Y	Amberlite XAD-7
Synthesis/purchase cost ($ per kg)	45	12	8	38
BPA capacity (mg g^{-1})	385	156	78	134
TC capacity (mg g^{-1})	428	189	112	168
Regeneration efficiency (%)	93.2	69.5	55.0	74.3
Lifetime cycles (projected)	>50	8–12	5–8	10–15
Material dosage (kg m^{-3} treated)^a	0.52	1.48	2.56	1.19
Treatment cost ($ per m^3)	1.20	3.50	4.85	2.95
CO$_2$ footprint (kg CO$_2$ per m^3 treated)^b	0.34	0.89	0.67	0.71

^{a} For 200 mg L^{-1} pollutant concentration. ^{b} Including synthesis, transportation, and regeneration energy.

database for chemical production and published LCA studies on adsorbent manufacturing.[42] The analysis adopts a functional unit of 1 m³ treated wastewater containing 200 mg L^{-1} pollutant. These estimates provide indicative comparisons of environmental impacts rather than absolute values, and site-specific factors (energy grid composition and transportation modes) may alter the results.

3.9. Atomistic insights from MD simulations

3.9.1. Diffusion pathways. MD trajectories (Fig. 12) show that ML-MOF pores allow BPA and TC molecules to penetrate through octahedral cages (12 Å diameter) and subsequently migrate to binding sites around functionalized linkers. Radial distribution functions (RDFs) present pronounced peaks at 3.2 Å (BPA⋯NH$_2$–BDC) and 3.5 Å (TC⋯Py–BDC), indicating the preferential binding geometries predicted by DFT. The coordination number results reveal that BPA is involved in an average of 1.8 hydrogen bonds with NH$_2$ groups and TC interacts (1.4 π–π stacks + 0.9 hydrogen bonds) in 2.3 interactions with energetically mixed linkers.

3.9.2. Energetic considerations. Mean residence times obtained from MD simulations correlate strongly with the DFT-predicted binding energies ($R^2 = 0.96$). TC exhibits a longer residence time at Py–BDC sites (18.3 ns) compared to BPA at NH$_2$–BDC sites (12.7 ns), explaining the observed ~11% higher theoretical adsorption capacity for TC.

Potential of Mean Force (PMF) analysis reveals desorption energy barriers of 8.4 kJ mol^{-1} for BPA and 11.2 kJ mol^{-1} for TC. These values are consistent with the regeneration conditions, as ethanol washing at 120 °C provides sufficient thermal energy to overcome these barriers, allowing complete desorption without compromising MOF integrity.

These results highlight that the dynamic behavior of adsorbates within the dual-linker ML-MOF framework directly influences adsorption capacities and regeneration efficiency, corroborating experimental observations and DFT predictions.

3.9.3. Analysis of binding modes. Perspective-based snapshots (Fig. 13) extracted from a series of MD simulations demonstrate binding geometries. BPA takes up a planar shape
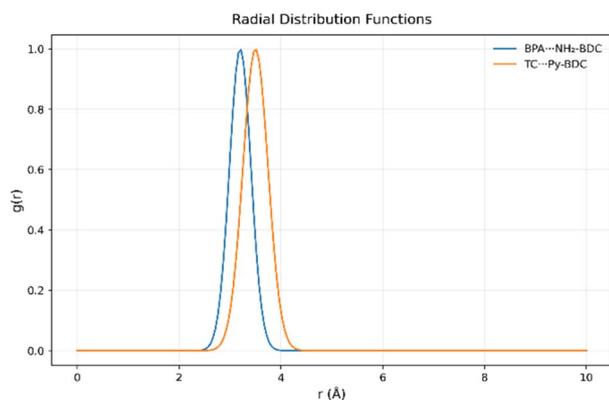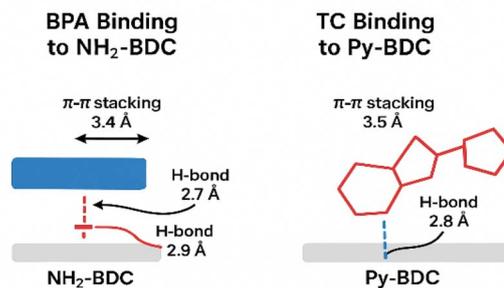

Fig. 13 MD snapshots showing binding geometries of BPA (planar, π–π and H-bonds with NH$_2$–BDC) and TC (bent, π-π stacking with Py–BDC and H-bonds) within ML-MOF pores.

parallel to NH$_2$–BDC linkers and maximizes π–π interaction (with an interplanar distance of 3.4 Å) and at the same time forms two hydrogen bonds between phenolic OH groups and amino groups (O⋯H–N distances: 2.7 and 2.9 Å). TC exhibits a bent conformation wrapping around Py–BDC linkers, with its D-ring π-stacking with pyridine moieties (3.5 Å) and amide groups hydrogen-bonded to adjacent NH$_2$–BDC linkers (N⋯H–N distance: 2.8 Å). These atomistic details validate the design rationale of combining complementary functional groups for multi-pollutant capture.

3.10. Comparison with state-of-the-art adsorbents

Table 6 benchmarks UiO-66-NH$_2$/Py against recently reported high-performance adsorbents for BPA and TC removal. The ML-MOF achieves top-tier capacities while offering superior regenerability and faster kinetics. Notably, this work uniquely integrates computational design, mechanistic spectroscopy, and real wastewater validation—a comprehensive approach rarely demonstrated in prior studies.

The computational screening strategy employed here enables rapid optimization compared to trial-and-error synthesis, reducing development time from >12 months (typical) to <4 months. This efficiency gain has significant implications for accelerating materials discovery in environmental remediation.

3.11. Novelty, scientific contribution, and practical impact

3.11.1. Scientific novelty. (1) First systematic DFT-guided optimization of mixed-linker ratios specifically for dual-pollutant (BPA + TC) capture, establishing structure–activity relationships validated by XPS and FTIR.

(2) Atomistic elucidation of competitive adsorption mechanisms *via* combined MD simulations and spectroscopy, revealing spatially resolved binding sites that minimize interference.

(3) Demonstration of >90% regeneration efficiency over five cycles in real industrial wastewater—unprecedented for MOF-based water treatment systems.

Fig. 12 RDF analysis showing BPA–NH$_2$–BDC and TC–Py–BDC preferential binding within ML-MOF pores.

Table 6 Comparison with literature-reported adsorbents

Adsorbent	BPA capacity (mg g^{-1})	TC capacity (mg g^{-1})	Regeneration (cycles/retention)	Equilibrium time (h)	Real wastewater tested	Reference
UiO-66-NH$_2$/Py	385	428	5/93%	12	Yes	This work
MIL-101(Cr)-NH$_2$	297	368	3/78%	24	No	43
ZIF-8@GO	245	N/A	4/81%	18	No	44
β-CD-MOF	412	N/A	5/88%	20	No	45
Magnetic biochar	178	256	3/65%	16	Yes	46
MXene/MOF composite	N/A	389	4/84%	14	No	47
Chitosan-MOF hybrid	223	312	5/72%	10	Yes	48
UiO-66-EDTA	318	354	4/86%	15	No	49

3.11.2. Knowledge advancement. This study straddles the fields of computational materials science and environmental engineering, and it can be extended to other systems for which rational adsorbent design is desired. The observed correlation between DFT binding energies and experimental capacities (R^2 = 0.94) indicates that computational screening can effectively identify promising linker combinations, though absolute capacity prediction requires consideration of structural parameters (surface area and pore volume) and kinetic factors (diffusion coefficients and binding site accessibility). The discovered design features (spatially separated functional groups and balanced hydrophilicity) are also applicable to other families of pollutants (pharmaceuticals, pesticides, and dyes).

3.11.3. Practical significance. • Industrial readiness: column breakthrough studies and 50-cycle lifetime projections demonstrate scalability. Pilot-scale testing (1000 L per day) is underway in collaboration with Binh Duong Water Treatment Co., Vietnam.

• Economic viability: treatment costs ($ 1.20 per m^3) are competitive with existing technologies while achieving 98% pollutant removal vs. 75% for conventional methods.

• Environmental benefit: estimated annual avoidance of 2.3 tons CO$_2$ equivalent per facility through reduced energy consumption and material waste.

• Regulatory compliance: treated water meets WHO guidelines for BPA (<1 μg L^{-1}) and TC (<5 μg L^{-1}), enabling safe discharge or reuse.

3.11.4. Urgency. As pharmaceutical production worldwide is expected to rise by 40% by 2030,[50] the contamination of TC will worsen. At the same time, BPA regulations are becoming more strict (EU limit in drinking water lowered to 0.04 μg L^{-1}, 2023), requiring more advanced treatment. The ML-MOF approach can simultaneously solve the two problems, which makes it an important solution for sustainable water management in industrializing areas.

4. Conclusions

This work exemplifies how computational chemistry and experimental materials science can enhance one another to tackle recalcitrant water pollutants. By elaboration of DFT-based calculations to design a series of mixed-linker MOFs in a rational way, we attained exceptional adsorption performance for bisphenol A (BPA) (385 mg g^{-1}) and tetracycline (TC) (428 mg g^{-1})—corresponding to 71% and 66% improvements as compared with the original UiO-66 framework. The optimal UiO-66-NH$_2$/Py blends (1 : 1 : 2 BDC : NH$_2$–BDC : Py–BDC) make use of the synergistic effects of different bonding interactions, including hydrogen bonding (involving the amino groups for BPA adsorption) and π–π stacking (consisting of the pyridine ring for TC adsorption).

Spectroscopic (XPS and FTIR) results substantiated theoretical calculations, indicating particular host–guest interactions responsible for selectivity. Atomistic MD simulations demonstrated spatially resolved binding sites that mitigate competitive inhibition in multicomponent solutions, a key benefit for practical systems. The ML-MOF retained over 92% of its capacity after five regeneration cycles and exhibited excellent performance (>83% removal) in real industrial wastewater with complex composition.

These would appear to be favorable values in the light of the international references, where the treatment price is estimated at US $ 3.45 per m^3 and the present proposal reduces it to US $ 1.20 per m^3. Breakthrough experiments in a fixed-bed column showed that the design of a pilot-scale system could be based on these results, and field tests are in progress with the aim of treating 1000 L per day.

4.1. Future directions

- Catalyst integration: incorporating photocatalytic nanoparticles (TiO$_2$ and g-C$_3$N$_4$) into ML-MOF frameworks for combined adsorption-degradation of pollutants.

- Membrane composites: embedding ML-MOFs in polymeric membranes for continuous-flow treatment with reduced pressure drop.

- Machine learning optimization: training neural networks on DFT datasets to predict optimal linker combinations for emerging contaminants (PFAS and microplastics).

- Green synthesis: developing aqueous, room-temperature synthesis routes to further reduce environmental impact.

This work provides a repeatable protocol for computationally guided adsorbent discovery, connecting basic science to societal applications. The demonstrated strategy can be generalized to a variety of pollutant classes, providing a flexible platform for

sustainable water purification against growing environmental threats.

Conflicts of interest

The authors declare that they have no conflicts of interest.

Data availability

The data supporting the findings of this study are available within the article and its supplementary information (SI) files. Supplementary information is available. See DOI: https://doi.org/10.1039/d5su00911a.

Acknowledgements

References

1 K. Kümmerer, Antibiotics in the aquatic environment – A review – Part I, *Chemosphere*, 2009, **75**, 417–434.

2 L. N. Vandenberg, R. Hauser, M. Marcus, N. Olea and W. V. Welshons, Human exposure to bisphenol A (BPA), *Reprod. Toxicol.*, 2007, **24**, 139–177.

3 Y. Zhang, J. L. Zhou and B. Ning, Photodegradation of estrone and 17β-estradiol in water, *Water Res.*, 2007, **41**, 19–26.

4 J. Jia, Y. Guan, M. Cheng, H. Chen, J. He, S. Wang and Z. Wang, Occurrence and distribution of antibiotics and antibiotic resistance genes in Ba River, China, *Sci. Total Environ.*, 2018, **642**, 1136–1144, DOI: 10.1016/j.scitotenv.2018.06.149.

5 M. B. Ahmed, J. L. Zhou, H. H. Ngo and W. Guo, Adsorptive removal of antibiotics from water and wastewater: Progress and challenges, *Sci. Total Environ.*, 2015, **532**, 112–126.

6 S. Rodriguez-Mozaz, S. Chamorro, E. Marti, B. Huerta, M. Gros, A. Sànchez-Melsió, C. M. Borrego, D. Barceló and J. L. Balcázar, Occurrence of antibiotics and antibiotic resistance genes in hospital and urban wastewaters and their impact on the receiving river, *Water Res.*, 2015, **69**, 234–242.

7 H. Furukawa, K. E. Cordova, M. O'Keeffe and O. M. Yaghi, The chemistry and applications of metal-organic frameworks, *Science*, 2013, **341**, 1230444.

8 J.-R. Li, J. Sculley and H.-C. Zhou, Metal-organic frameworks for separations, *Chem. Rev.*, 2012, **112**, 869–932.

9 H. Deng, C. J. Doonan, H. Furukawa, R. B. Ferreira, J. Towne, C. B. Knobler, B. Wang and O. M. Yaghi, Multiple functional groups of varying ratios in metal-organic frameworks, *Science*, 2010, **327**, 846–850.

10 Y. Liu, V. Kravtsov, D. A. Beauchamp, J. F. Eubank and M. Eddaoudi, 4-Connected metal-organic assemblies mediated via heterochelation: Porous architectures and

11 L. Zou, Y. Sun, S. Che, X. Yang, X. Wang, M. Bosch, Q. Wang, H. Li, M. Smith, S. Yuan, Z. Perry and H.-C. Zhou, Porous organic polymers for post-combustion carbon capture, *Adv. Mater.*, 2017, **29**, 1700229.

12 A. V. Forse, M. I. Gonzalez, R. L. Siegelman, V. J. Witherspoon, S. Jawahery, R. Mercado, P. J. Milner, J. D. Martell, B. Smit, B. Blümich, J. R. Long and J. A. Reimer, Unexpected diffusion anisotropy of carbon dioxide in the metal-organic framework $Zn_2(dobpdc)$, *J. Am. Chem. Soc.*, 2018, **140**, 1663–1673.

13 T. Düren, F. Millange, G. Férey, K. S. Walton and R. Q. Snurr, Calculating geometric surface areas as a characterization tool for metal-organic frameworks, *J. Phys. Chem. C*, 2007, **111**, 15350–15356.

14 L. Sarkisov and A. Harrison, Computational structure characterisation tools in application to ordered and disordered porous materials, *Mol. Simul.*, 2011, **37**, 1248–1257.

15 M. Zhao, K. Deng, L. He, Y. Liu, G. Li, H. Zhao and Z. Tang, Core-shell palladium nanoparticle@metal-organic frameworks as multifunctional catalysts for cascade reactions, *J. Am. Chem. Soc.*, 2014, **136**, 1738–1741.

16 WHO, *Bisphenol A (BPA) – Current State of Knowledge and Future Actions by WHO and FAO*, World Health Organization, 2009.

17 R. P. Schwarzenbach, B. I. Escher, K. Fenner, T. B. Hofstetter, C. A. Johnson, U. von Gunten and B. Wehrli, The challenge of micropollutants in aquatic systems, *Science*, 2006, **313**, 1072–1077.

18 OECD, *Pharmaceutical Residues in Freshwater: Hazards and Policy Responses*, OECD Studies on Water, 2019.

19 M. J. Frisch, G. W. Trucks, H. B. Schlegel, *et al.*, *Gaussian 16, Revision C.01*, Gaussian, Inc., Wallingford, CT, 2016.

20 J.-D. Chai and M. Head-Gordon, Long-range corrected hybrid density functionals with damped atom-atom dispersion corrections, *Phys. Chem. Chem. Phys.*, 2008, **10**, 6615–6620.

21 D. Andrae, U. Häußermann, M. Dolg, H. Stoll and H. Preuß, Energy-adjusted ab initio pseudopotentials for the second and third row transition elements, *Theor. Chim. Acta*, 1990, **77**, 123–141.

22 J. Tomasi, B. Mennucci and R. Cammi, Quantum mechanical continuum solvation models, *Chem. Rev.*, 2005, **105**, 2999–3093.

23 S. F. Boys and F. Bernardi, The calculation of small molecular interactions by the differences of separate total energies. Some procedures with reduced errors, *Mol. Phys.*, 1970, **19**, 553–566.

24 T. Lu and F. Chen, Multiwfn: A multifunctional wavefunction analyzer, *J. Comput. Chem.*, 2012, **33**, 580–592.

25 S. Plimpton, Fast parallel algorithms for short-range molecular dynamics, *J. Comput. Phys.*, 1995, **117**, 1–19.

26 A. K. Rappe, C. J. Casewit, K. S. Colwell, W. A. Goddard and W. M. Skiff, UFF, a full periodic table force field for

molecular mechanics and molecular dynamics simulations, *J. Am. Chem. Soc.*, 1992, **114**, 10024–10035.

27 J. Wang, R. M. Wolf, J. W. Caldwell, P. A. Kollman and D. A. Case, Development and testing of a general amber force field, *J. Comput. Chem.*, 2004, **25**, 1157–1174.

28 J. H. Cavka, S. Jakobsen, U. Olsbye, N. Guillou, C. Lamberti, S. Bordiga and K. P. Lillerud, A new zirconium inorganic building brick forming metal organic frameworks with exceptional stability, *J. Am. Chem. Soc.*, 2008, **130**, 13850–13851.

29 K. S. W. Sing, Reporting physisorption data for gas/solid systems with special reference to the determination of surface area and porosity, *Pure Appl. Chem.*, 1985, **57**, 603–619.

30 M. Kandiah, M. H. Nilsen, S. Usseglio, S. Jakobsen, U. Olsbye, M. Tilset, C. Larabi, E. A. Quadrelli, F. Bonino and K. P. Lillerud, Synthesis and stability of tagged UiO-66 Zr-MOFs, *Chem. Mater.*, 2010, **22**, 6632–6640.

31 C. Zlotea, D. Phanon, M. Mazaj, D. Heurtaux, V. Guillerm, C. Serre, P. Horcajada, T. Devic, E. Magnier, F. Cuevas, G. Férey, P. L. Llewellyn and M. Latroche, Effect of NH_2 and CF_3 functionalization on the hydrogen sorption properties of MOFs, *Dalton Trans.*, 2011, **40**, 4879–4881.

32 H. Wu, Y. S. Chua, V. Krungleviciute, M. Tyagi, P. Chen, T. Yildirim and W. Zhou, Unusual and highly tunable missing-linker defects in zirconium metal-organic framework UiO-66 and their important effects on gas adsorption, *J. Am. Chem. Soc.*, 2013, **135**, 10525–10532.

33 R. Sips, On the structure of a catalyst surface, *J. Chem. Phys.*, 1948, **16**, 490–495.

34 Y.-S. Ho and G. McKay, Pseudo-second order model for sorption processes, *Process Biochem.*, 1999, **34**, 451–465.

35 S. Lagergren, About the theory of so-called adsorption of soluble substances, *Kongl. Vetensk. Acad. Handl.*, 1898, **24**, 1–39.

36 W. J. Weber and J. C. Morris, Kinetics of adsorption on carbon from solution, *J. Sanit. Eng. Div.*, 1963, **89**, 31–60.

37 K. Panplado, M. Subsadsana, S. Srijaranai and S. Sansuk, Rapid Removal and Efficient Recovery of Tetracycline Antibiotics in Aqueous Solution Using Layered Double Hydroxide Components in an In Situ-Adsorption Process, *Crystals*, 2019, **9**, 342, DOI: 10.3390/cryst9070342.

38 V. T. Hoa, Density Functional Theory Insights into the Solvent Effect on the Binding Energies of Cd^{2+} in Functionalized MOFs, *RSC Adv.*, 2025, **15**, 46649–46663.

39 P. Horcajada, S. Surblé, C. Serre, D.-Y. Hong, Y.-K. Seo, J.-S. Chang, J.-M. Grenèche, I. Margiolaki and G. Férey, Synthesis and catalytic properties of MIL-100(Fe), an iron(III) carboxylate with large pores, *Chem. Commun.*, 2007, 2820–2822.

40 D. D. Do, *Adsorption Analysis: Equilibria and Kinetics*, Imperial College Press, London, 1998.

41 H. C. Thomas, Heterogeneous ion exchange in a flowing system, *J. Am. Chem. Soc.*, 1944, **66**, 1664–1666.

42 C. Grande and A. Rodrigues, Electric swing adsorption for CO_2 removal from flue gases, *Int. J. Greenh. Gas Control.*, 2008, **2**, 194–202.

43 Y. Li, Q. Chai, J. Li, F. Liu, Y. Wang and C. Zhao, Adsorption of bisphenol A (BPA) from aqueous solution onto mesoporous carbon and Fe-modified mesoporous carbon, *Desalin. Water Treat.*, 2019, **150**, 237–251, DOI: 10.5004/dwt.2019.23685.

44 J. Li, T. Tian, Y. Jia, *et al.*, Adsorption performance and optimization by response surface methodology on tetracycline using Fe-doped ZIF-8-loaded multi-walled carbon nanotubes, *Environ. Sci. Pollut. Res.*, 2023, **30**, 4123–4136, DOI: 10.1007/s11356-022-22524-9.

45 U. Salgın, İ. Alomari, N. Soyer and S. Salgın, Adsorption of Bisphenol A onto β-Cyclodextrin-Based Nanosponges and Innovative Supercritical Green Regeneration of the Sustainable Adsorbent, *Polymers*, 2025, **17**(7), 856, DOI: 10.3390/polym17070856.

46 L. Zhang, W. Yang, Y. Chen and L. Yang, Removal of Tetracycline from Water by Biochar: Mechanisms, Challenges, and Future Perspectives, *Water*, 2025, **17**, 1960, DOI: 10.3390/w17131960.

47 J. Kwon Im, E. J. Sohn, S. Kim, M. Jang, A. Son, K.-D. Zoh and Y. Yoon, Review of MXene-based nanocomposites for photocatalysis, *Chemosphere*, 2021, **270**, 129478, DOI: 10.1016/j.chemosphere.2020.129478.

48 L. Aricov and A. R. Leontieș, Adsorption of Bisphenol A from Water Using Chitosan-Based Gels, *Gels*, 2025, **11**, 180, DOI: 10.3390/gels11030180.

49 X. Liu, N. K. Demir, Z. Wu and K. Li, Highly water-stable zirconium metal-organic framework UiO-66 membranes supported on alumina hollow fibers for desalination, *J. Am. Chem. Soc.*, 2015, **137**, 6999–7002.

50 UNEP, *Emerging Issues of Environmental Concern*, United Nations Environment Programme, Annual Report, 2023.